Electronic supplementary Information

COOH-Terminated Nitrogen-Doped Carbon Aerogel as Bulk Electrode for Completely Selective Two-Electron Oxygen Reduction to H_2O_2

Hongying Zhao,*[a,b] Xuqian Shen,[a] Ying Chen,[a] Shi-Nan Zhang,[c] Peng Gao,[c] Xiangjun Zhen,[d] Xin-Hao Li, *[c] and Guohua Zhao*[a]

[a] School of Chemical Science and Engineering, and Shanghai Key lab of Chemical Assessment and Sustainability, Tongji University, Shanghai 200092, P.R. China;

[b] Nanjing University& Yancheng Academy of Environmental Protection Technology and Engineering Yancheng 224001, P. R. China;

[c] School of Chemistry and Chemical Engineering, Shanghai Jiao Tong University, Shanghai 2000240, P.R. China;

[d] Shanghai Institute of Applied physics, Chinese Academy of Science, Shanghai 201204, P.R. China.

Corresponding author:

Hongying Zhao; Address: School of Chemical Science and Engineering, and Shanghai Key lab of Chemical Assessment and Sustainability, Tongji University, Shanghai 200092, P.R. China; Email: hyzhao@tongji.edu.cn; Fax: +86 21 65982287, Tel.: +86 2165988570.

Guohua Zhao; Address: School of Chemical Science and Engineering, and Shanghai Key lab of Chemical Assessment and Sustainability, Tongji University, Shanghai 200092, P.R. China; Email: g.zhao@tongji.edu.cn; Fax: +86 21 65982287, Tel.: +86 2165981180.

Xin-Hao Li; Address: School of Chemistry and Chemical Engineering, Shanghai Jiao Tong University, Shanghai 200240, P.R. China; Email: xinhaoli@sjtu.edu.cn.

1. Experimental Procedures

All chemicals were used without any further purification. $HClO_4$ (AR, 70%), H_2SO_4 (AR, 98%), Resorcinol (AR, 99.5%), ethanol (AR, 99.7%), acetone (AR, 99.7%), Na_2SO_4 (AR, 99%) and KOH (AR, 85%) were purchased from Sinopharm Group chemical Reagent Co., Ltd. Titanium oxysulfate (29%) were purchased from Sigma-Aldrich. Acetonitrile (GR, 99.9%) wre purchased from Germany Merck KgaA. Formaldehyde solution (AR, 37%, contains 7% methanol stabilizer) were purchased from Aladdin .

1.1 Preparation of N-doped carbon aerogel electrodes

Resorcinol, formaldehyde, deionized water, and sodium carbonate were mixed, after forming a homogeneous solution, the mixture was cast into a cuboid glass with the interlayer distance of 5 mm, and cured at 30 °C for one day, 50 °C for one day, and 90 °C for 3 days. The given amount of acetonitrile as nitrogen precursors were introduced during the synthesis of carbon aerogel for obtaining N-doped carbon aerogel (NCA). The resulting organic wet gel was immersed in acetone for 3 days in order to replace the water in the wet gel, then, it was dried under ambient condition for 4 days to obtain massive dry gel with integrated structure. Then wet gel was treated in N_2 with a flow rate of 200 mL min^{-1}, followed by using a heating rate of 5^{o} C min^{-1} from ambient temperature to 650 °C and kept for 2 h, and then cooled to ambient temperature. The NCA-x was further activated by changing the synthetic temperatures (x: 750, 850 and 950 °C). For comparation, the pure carbon aerogel (CA) was prepared according with the same procedures without adding acetonitrile.

1.2 Characterization methods

The N_2 adsorption–desorption analysis was performed on Micromeritics ASAP 2460 instrument. All the samples were degassed at 573 K overnight before each measurement. The Brunauer-Emmet-Teller (BET) special surface area was calculated by choosing N_2 adsorption data from relative pressure from 0.05 to 0.2. The morphology of obtained electrodes was characterized by scanning electron microscopy (SEM, Hitachi-S4800). Surface functional groups of the materials were investigated using Fourier transform infrared (FTIR) spectroscopy using a Thermo Scientific Nicolet IS10 spectrophotometer. The materials were mixed with KBr powder in a ratio of 1:200 and measured under a dry air purging environment. X-ray photoelectron spectroscopy (XPS) measurement was carried out with a Kratos AXIS-HS using a focused monochromatic Al Kα X-ray radiation (150 W, 15 kV, 10 mA). The binding energy scale was calibrated by using the value of the C1s peak at 284.6 eV. The compressive strengths of materials were performed by a tensile-compressive tester (FR-103C, Farui Co.). The compression rate is 2 mm/min. The Element Analysis (EA) was detected by Vario EL Cube equipped with M5X analytical balance. The soft X-ray adsorption spectroscopy data at O K-edges were collected at room temperature at BL08U1A beamline of Shanghai Synchrotron Radiation Facility (SSRF). The acquired NEXAFS data were normalized using the ATHENA module implemented in the IFEFFIT software packages. The temperature-programed desorption (TPD) measurements using an Auto Chem II 2920 instrument (Micromeritics) was used to estimate the amount of adsorbed oxygen and the strength of adsorption on electrode surfaces. 100 mg of the catalyst was dosed with O_2/He (10% v/v) to saturation of O_2 adsorption at 35 ^{o}C. Subsequently, helium gas was purged for 1 h to remove weakly adsorbed species. Finally, the catalysts were heated in the flowing helium by ramping the temperature from 35 to 700 ^{o}C at a rate of 10 ^{o}C/min.

1.3 Electrochemical property test

The oxygen reduction reaction (ORR) was examined using a Pine AFMSRXE 1523. First, 10 mg of catalysts were added into a mixture of 1.5 mL of water, 0.75mL of ethanol and a 0.25 mL nafion solution (5 wt.%, Alfar Aesar). A homogenous suspension ink was obtained by using ultrasonic oscillation for 60 min. A 12–μL ink aliquot was dropped onto a glassy carbon (GC) disk electrode for RRDE test, respectively. The RRDE is composed of a 5.61 mm diameter GC disk (0.248cm^2) and Pt ring (0.187 cm^2) (its collection efficiency is 0.37). The loading density of catalyst in RRDE was 196 μg cm^{-2}. The working electrodes were finally synthesized after drying at ambient temperature for 12 h.

For the measurement of the oxygen reduction reaction (ORR), the electrochemical analysis of the working electrodes containing the catalysts were performed on a computer–controlled CHI 760E electrochemical station (Chenhua Instrument Co. Ltd., China) with a traditional three–electrode system in 100 mM KOH solution and 100 mM $HClO_4$ solution at 25°C. KOH and $HClO_4$ is a nonadsorbing electrolyte and it will not compete with the oxygen intermediates for surface adsorption. A platinum wire and a KCl–saturated Hg/Hg_2Cl_2 electrode were used as the counter electrode and the reference electrode, respectively. In the alkaline solution, before all electrochemical experiments, cyclic voltammetry (CV) was recorded in N_2–saturated 100 mM KOH solution between +0.3 to +0.9 V at a sweep rate of 50 mV s^{-1} until to get a stable electrochemical profile. Similarly, the Pt ring electrode was also treated with a potential scanning from -0.2 to +0.4 V at 50 mV s^{-1}. For the CV measurement, it's were carried out in N_2 and O_2-saturated 0.1M KOH with a scan rate of 10 mVs^{-1}. For each rotating ring-disk electrode (RRDE) test in KOH electrolyte, linear sweep voltammetry (LSV) was performed in N_2–saturated solution at different applied voltages from +0.3 to +0.9 V at a sweep rate of 1 mV s^{-1} and then performed in O_2–saturated solution under the same operational conditions. The Pt ring electrode was fixed at a constant potential of +1.3 V vs RHE to oxidize product H_2O_2, produced at the disk and swept over to the ring by the radial flow. In $HClO_4$ solution, the RRDE test potential is -0.2V to 0.3V and the Pt ring electrode was fixed at 2.2 V vs RHE. The rest are the same with KOH solution. The differential values in LSV–derived current density with O_2–saturated electrolyte and in N_2–saturated electrolyte was regarded as the ORR current density of the catalysts. The selectivity of H_2O_2 can be calculated according to equation:

$$H_2O_2 \text{ (yield): } H_2O_2(\%) = 200 \times \frac{I_R/N}{I_D + (I_R/N)} \qquad (1)$$

Where I_R is the ring electrode current, I_D is the disk electrode current, and N is the ring electrode collection efficiency (0.37).

1.4 The electrogeneration of H_2O_2

The electrogeneration of H_2O_2 were conducted in two electrode system in a two-compartment cell with nafion 117 membrane as separator. Both the cathode compartment (50ml) and anode compartment (50 mL) were filled with the same electrolyte at 25 °C. For H_2O_2 production, the CA and NCA series electrode (working area of 3 cm^2) were directly used as work cathodes, and Pt foil with the same area was used as the anode; the distance between the two electrodes was 7 cm. The electrolyte was 50 mM Na_2SO_4 solution at pH=3 which was adjusted with 100 mM of H_2SO_4. In two-compartment cell, the H_2O_2 yield was conducted current at 10, 20 and 30 mA with continuously O_2 feeding.

To quantify the H_2O_2 produced, the samples was collected at certain time and mixed with same volume of titanium oxysulfate solution (6 g L^{-1}). The H_2O_2 yield was measured by using the indicator of titanium oxysulfate. The generated complex compound solution was detected with UV−vis spectrophotometer (Agilent 8453, Agilent Corporation, U.S.) at

the maximum absorption wavelength λ=406 nm.

1.5 Computational studies

Spin-polarized density functional theory calculations were performed through the projector augmented wave (PAW)[1] method as implemented in the Vienna ab initio simulation package (VASP). Electron exchange–correlation was represented by the functional of Perdew, Burke and Ernzerhof (PBE) of generalized gradient approximation (GGA).[2] A cutoff energy of 500 eV for plane-wave basis set were adopted. The convergence threshold was 10^{-5} eV and 0.01 eV/Å for energy and force, respectively. The catalyst with periodic boundary condition was modeled with a large super cell of 20×20×15 Å,[3] eliminating the artificial interaction between electrocatalysts in adjacent cells. The Brillouin zone integrations were performed by using Gamma 1×1×1 for geometric optimization. DFT-D_3 calculations were used to describe the weak interaction.[4] The computational hydrogen electrode was used to obtain free energies for each state as done in previous paper.[5] The electroreduction of O_2 to H_2O_2 involves two coupled electron and proton transfers, which can be summarized by the following two elementary steps:

$$O_2 + * + (H^+ + e^{-1}) \rightarrow HOO* \quad (2)$$

$$HOO* + (H^+ + e^{-1}) \rightarrow H_2O_2 + * \quad (3)$$

Where the * and HOO* denotes the activity site and the adsorbed HOO intermediate on the catalyst, respectively. The entropy and zero-point energy were obtained by frequency calculation at 300K.[6]

Adsorption energy calculation was performed using density functional theory (DFT), as implemented in the DMol3 program. The DFT calculation was carried out by placing an oxygen molecule at the top of graphene structure linked with –N, –COOH and –(COOH+N) groups. The adsorption energy of oxygen (E_{ads}) was calculated using the following equation:

$$E_{ads} = E_{oxygen+catalyst} - E_{oxygen} - E_{catalyst} \quad (4)$$

2-3. Figures S1-S19 and Tables S1-S3

Table S1. The free energy for oxygen reduction to HOO*, theoretical over potential ($\eta O_2/H_2O_2$) for oxygen reduction to H_2O_2 and oxygen adsorption energy over typical carbon models with various functional groups as shown in Figure 1.

Functional group in carbon models	Free energy of HOO* (eV)	$\eta O_2/H_2O_2$ (V)	Oxygen adsorption energy (eV)
N	2.87	0.65	0.61
COOH	4.48	0.96	0.55
N+COOH	3.36	0.16	0.86
N+OH	2.74	0.78	--[a]

[a] not determined

To rationalize the synergetic effect of nitrogen dopants and oxygen functional groups on the catalytic performance of $2e^-$ ORR, the density functional theory (DFT) calculation were performed on the active sites (circle carbon atom in Figure 1) dominated with graphitic N, –COOH and –OH functionalities. The $2e^-$ reduction pathway to forming H_2O_2 involves the following reactions with HOO* as a reaction intermediate (eqs 1 and 2).

In fact, varying the catalyst is to tune the binding of HOO* to the surface. The binding energy of HOO*(ΔG_{HOO*}) is the key descriptor for controlling the catalytic activity in $2e^-$ ORR. The ideal catalyst for $2e^-$ ORR is determined to have a thermoneutral adsorption of sole reaction intermediate HOO* at equilibrium potential ($U^0_{O2/H2O2}$=0.7V).[7] Both stronger and weaker binding to HOO* would bring additional overpotential. Thus, the theoretical overpotential ($\eta O_2/H_2O_2$), indicated by blue arrow, presented a volcano-type dependence of ΔG_{HOO*} in Figure 1c. In all these configurations (Figure 1a), the ORR activity and selectivity are both varied when changing the local chemical environmental of active carbon atoms in graphene structure. C-COOH/C-N group imbedded carbon material has the least downhill in free energy to form H_2O_2. Accordingly, a minimum $\eta O_2/H_2O_2$ of 0.16 V is required to drive H_2O_2 formation. Nevertheless, the C–OH/ C-N group in carbon material does not contributed to ORR since the high value of $\eta O_2/H_2O_2$ (0.78V). The merely N group in carbon is 0.65 V downhill in free energy to form HOO*. The $\eta O_2/H_2O_2$ of carbon material merely linked with –COOH is 0.96 V, indicating the reaction involving more than two electrons.[8] This means the synergistic effect of C-COOH/C-N greatly improved the activity for $2e^-$ oxygen reduction. The interface between C atoms, linked with –COOH and nitrogen dopant is the key role for H_2O_2 formation.

The strong coordination effect between C-N and C-COOH group in bossting the oxygen adsorption was examined via theoretical and experimental methods.[9] Density functional theory (DFT) sumulation results reveal the favorable adsorption of oxygen on the surface of carbon framework embeeded with nitrogen dopants and COOH group, which results in most positive binding energy (0.86 eV) of oxygen for further promoting the ORR perfomance and H_2O_2 formation.

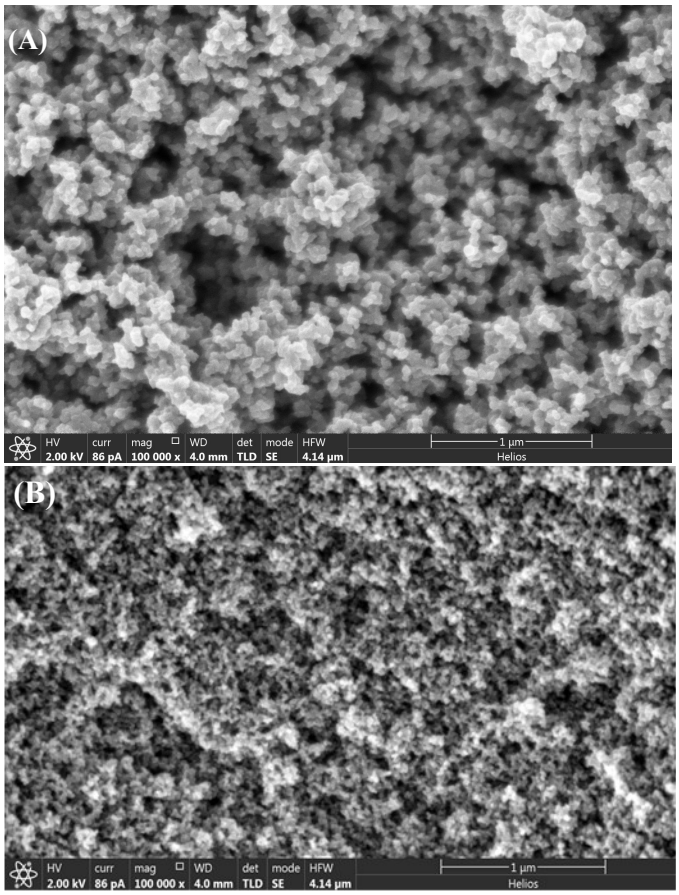

Figure S1. SEM images for (A) CA-850 and (B) NCA-850 electrodes.

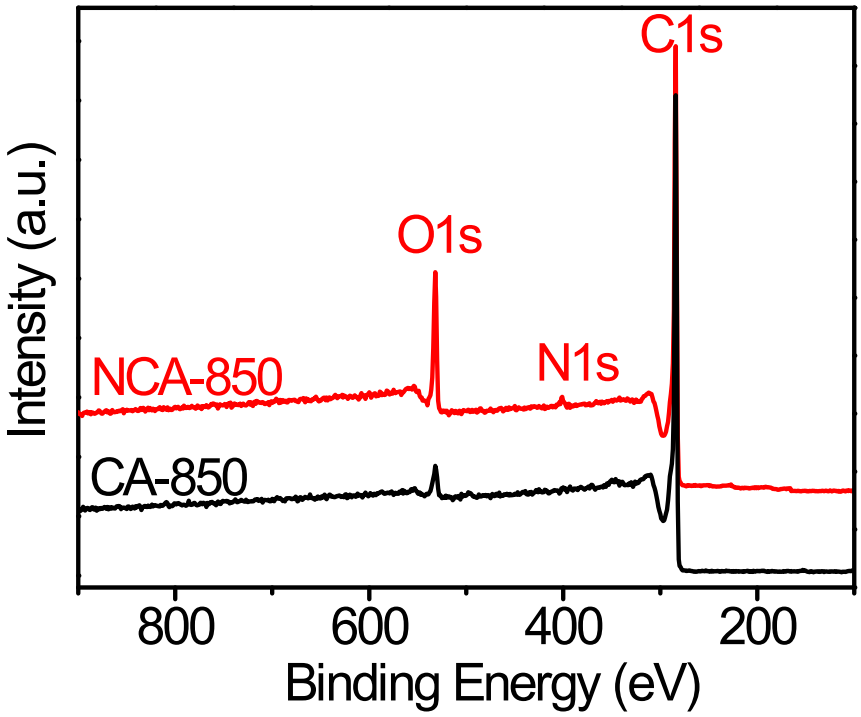

Figure S2. The XPS full spectrum survey scan for CA-850 and NCA-850 electrodes.

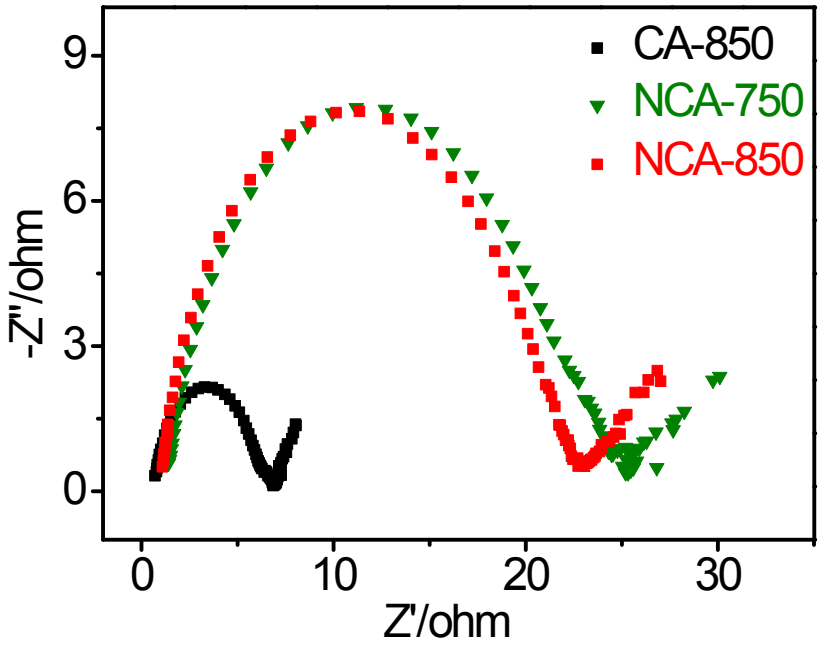

Figure S3. Electrochemical impedance spectroscopy of CA-850, NCA-750 and NCA-850 electrodes.

For the electrochemical impedance spectroscopy measurements, all tests are performed in mixed solution of 5 mM $Fe_3(CN)_6$ and 0.1M KCl. The electrochemical impedance of CA-850 is 8 Ω, indicating the excellent conductivity. After doped N atoms, the physical resistance of NCA series electrodes was increased. Anyhow, still presenting good conductivity. The physical resistance of NCA-750 and NCA-850 electrodes was respectively increased to 13 and 9 Ω/cm, and the electrochemical impedance was respectively increased to 25 and 22 Ω. High thermal treatment is beneficial to improve the conductivity of electrode. However, after 950°C calcination, the surface of NCA-950 was cracked and thus can't be directly used as work electrode. Thus, the physical resistance and electrochemical impedance of NCA-950 was not tested.

Table S2. The physical properties of NCA series electrode include XPS analysis, elemental analysis (EA), Brunner−Emmet−Teller (BET) measurement, physical resistance and electrochemical impendance measurement.

Sample	C	N	O	C	N	H	S_{BET} (m^2/g)	Resistance (Ω/cm)	Electrochemical Impendance (Ω)
	w.t.% (XPS)			w.t.% (EA)					
NCA-750	89.3	1.2	9.5	99.3	0.5	0.2	700	13	25
NCA-850	87.9	1.9	10.2	99.2	0.7	0.1	846	9	22
NCA-950	91.5	1.1	7.4	99.3	0.6	0.1	723	--[a]	--[a]

[a] Not determined since NCA-950 was cracked after 950°C calcination.

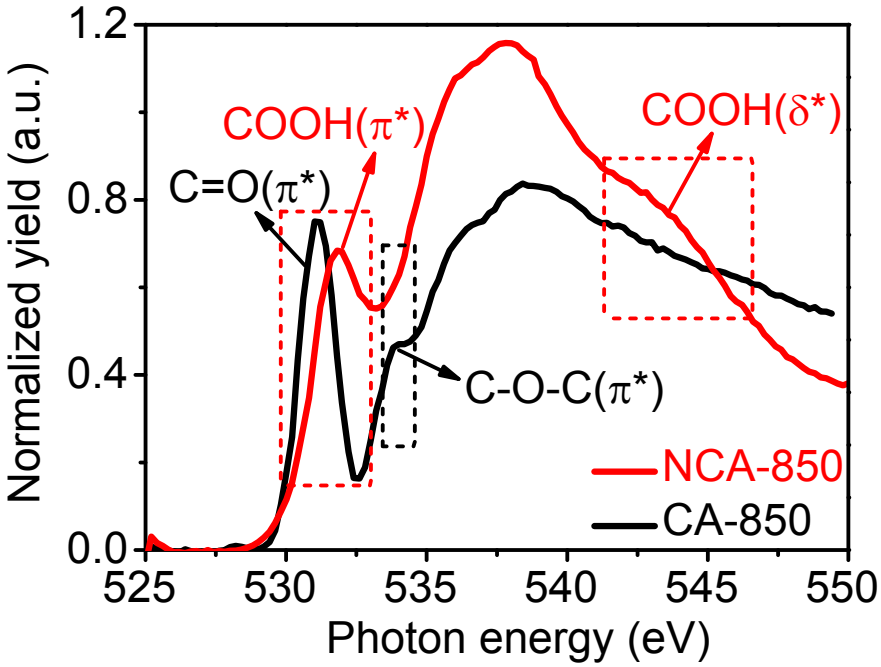

Fig S4. The NEXAFS of O K-edge of NCA-850 and CA-850 samples.

The O K-edge near-edge X-ray adsorption fine structure (NEXAFS) spectra demonstrated that the introduction of nitrogen promoted the formation of –COOH group. A sharp and intense peak ascribed to the π* of the –C=O at 531.0 eV moved to 532.0 eV, which is due to the generation of π* in –COOH after the introducing of nitrogen into the matrix of carbon. The O1s→π* peak near 534 eV associated with single bonded oxygen –C-O-C is observed in pure carbon aerogel electrode. A broad peak ranging from 535 to 550 eV was due to the O1s→σ* in the type of carbonyl species (both –COOH and –C=O). In addition, the σ* peak become more well defined in NCA, suggesting the loss of polydisperse oxygen species such as C–O–C species. A weak shoulder σ* peak near 543.6 eV arose for NCA that could originate for –COOH.[10]

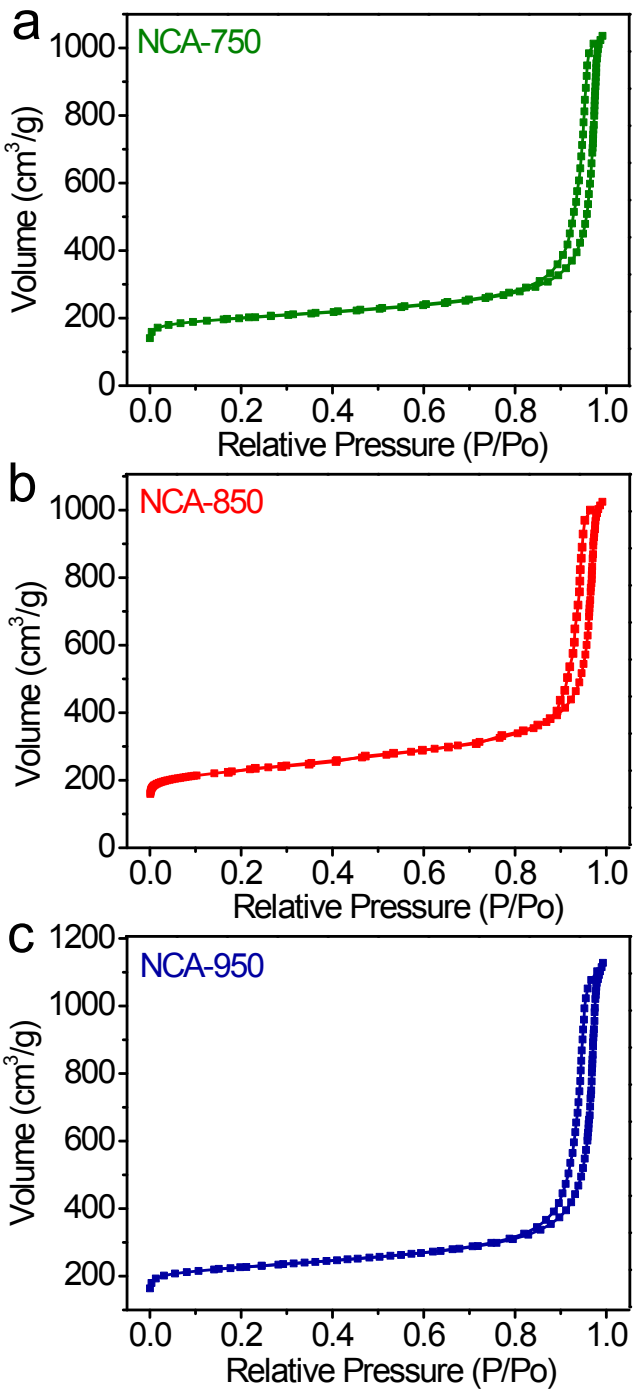

Figure S5. The N_2 adsorption isotherms of NCA-750, NCA-850 and NCA-950 samples.

The hysteresis (type H3 loop) in the isotherm can be observed for NCA-750, NCA-850 and NCA-950, which is associated with narrow slit-like pores. The thermal activation at different temperatures didn't change the porosity of nitrogen-doped carbon aerogel materials.

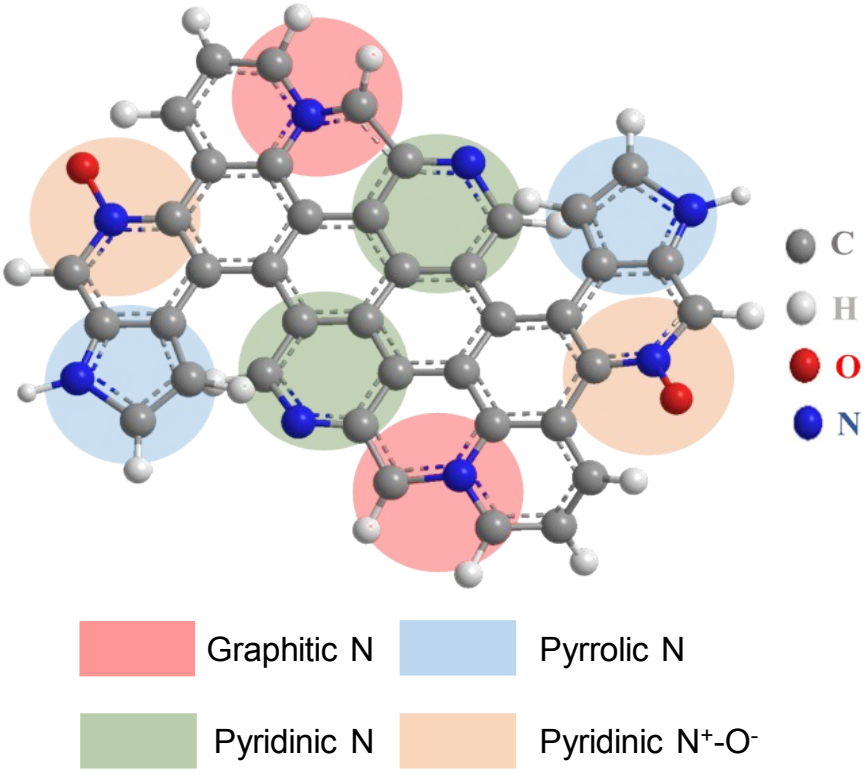

Figure S6. Schematic illustration of four types of nitrogen in nitrogen-doped carbon aerogel.

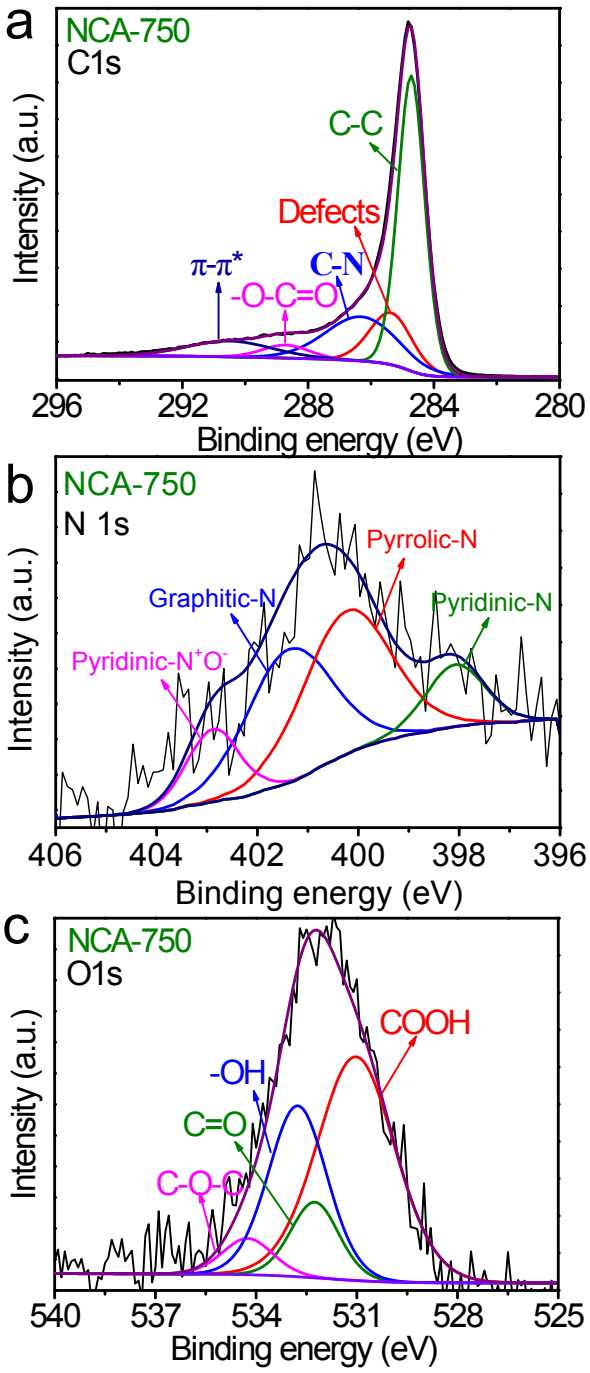

Figure S7. Multicomponent fits of the C 1s, O 1s and N 1s XPS spectra for NCA-750.

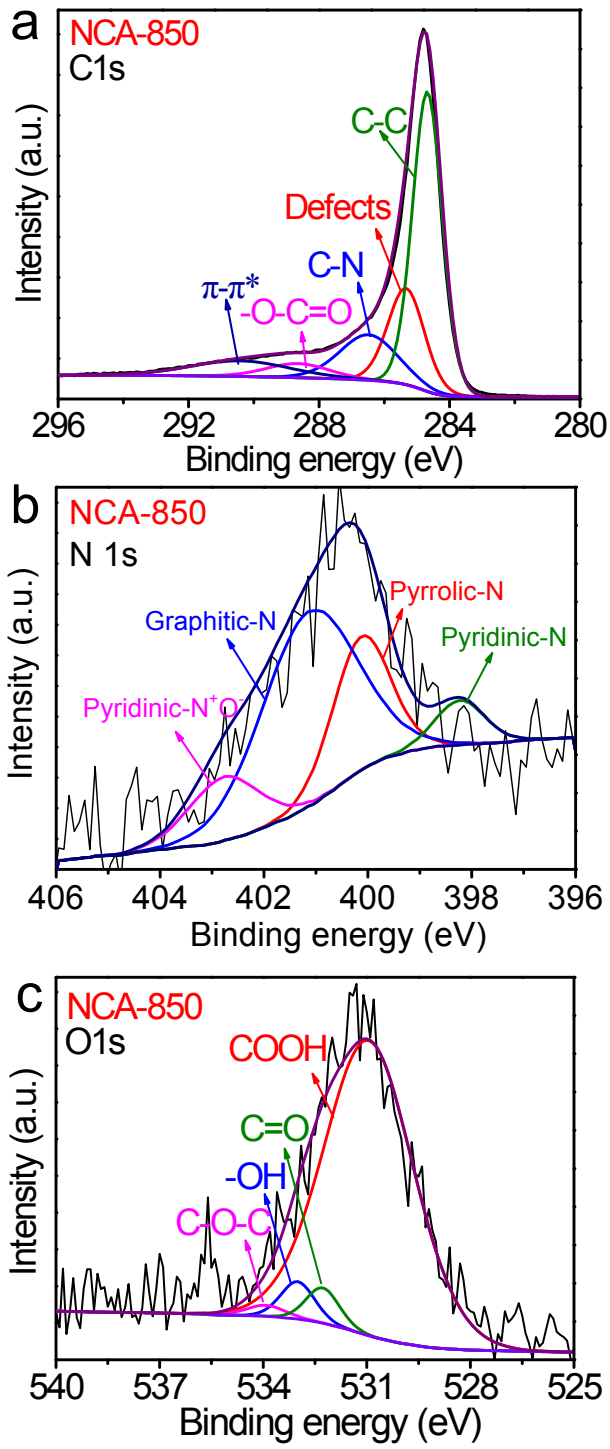

Figure S8. Multicomponent fits of the C 1s, O 1s and N 1s XPS spectra for NCA-850.

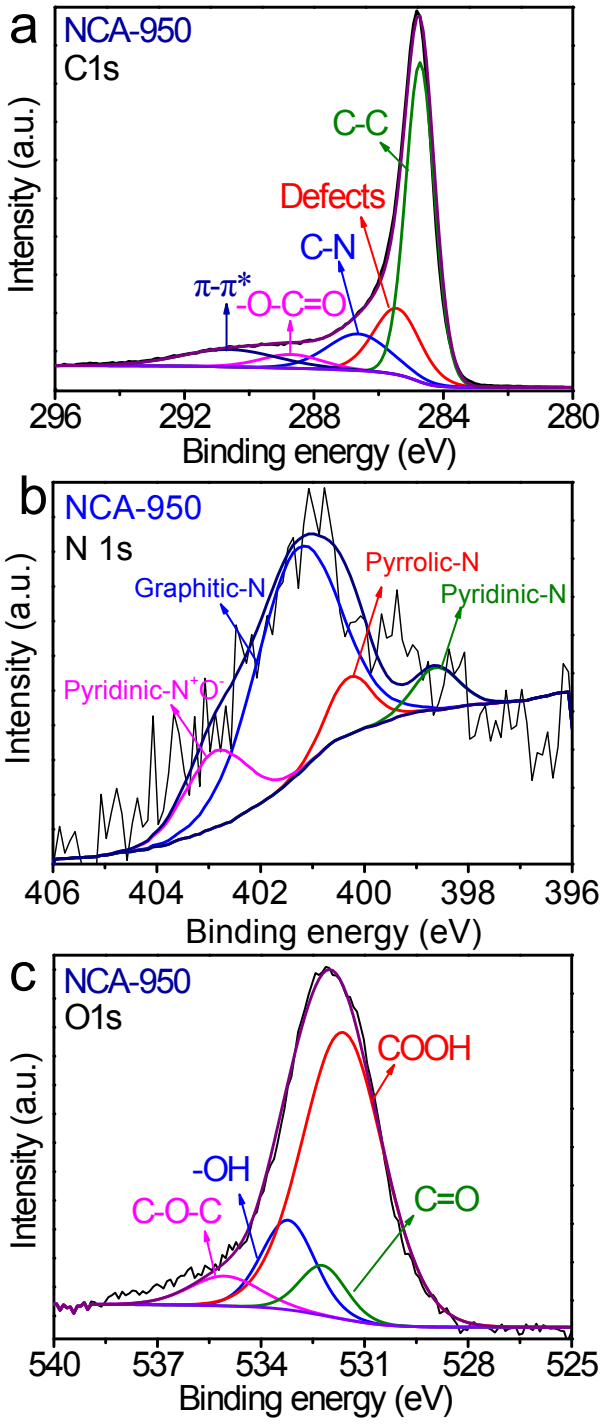

Figure S9. Multicomponent fits of the C 1s, O 1s and N 1s XPS spectra for NCA-950.

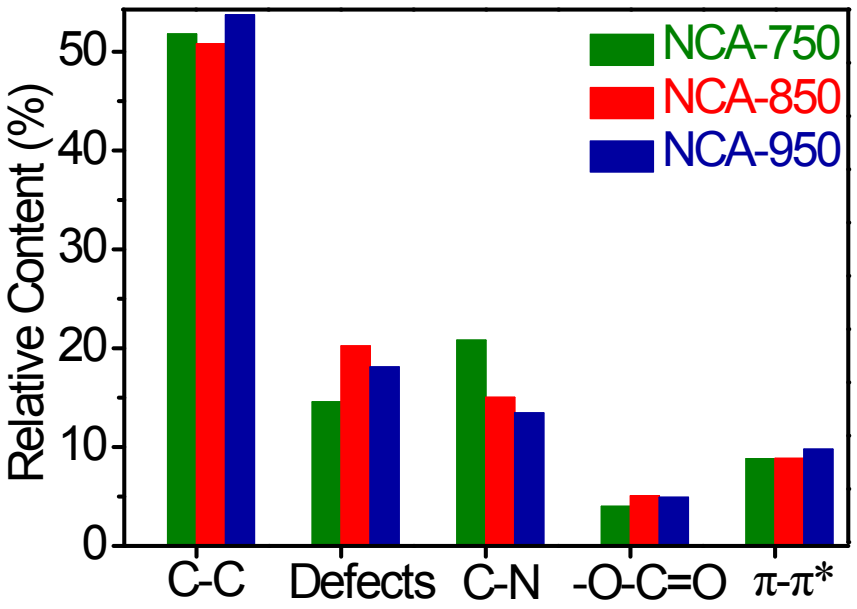

Figure S10. Relative content of deconvoluted C 1s XPS spectra for NCA-750, NCA-850 and NCA-950 samples.

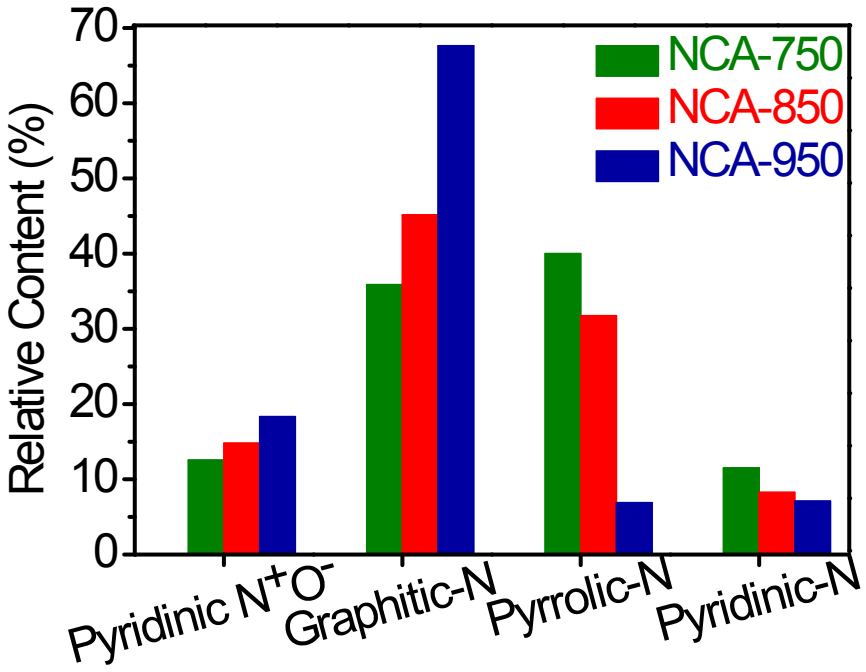

Figure S11. Relative content of deconvoluted N 1s XPS spectra for NCA-750, NCA-850 and NCA-950 samples.

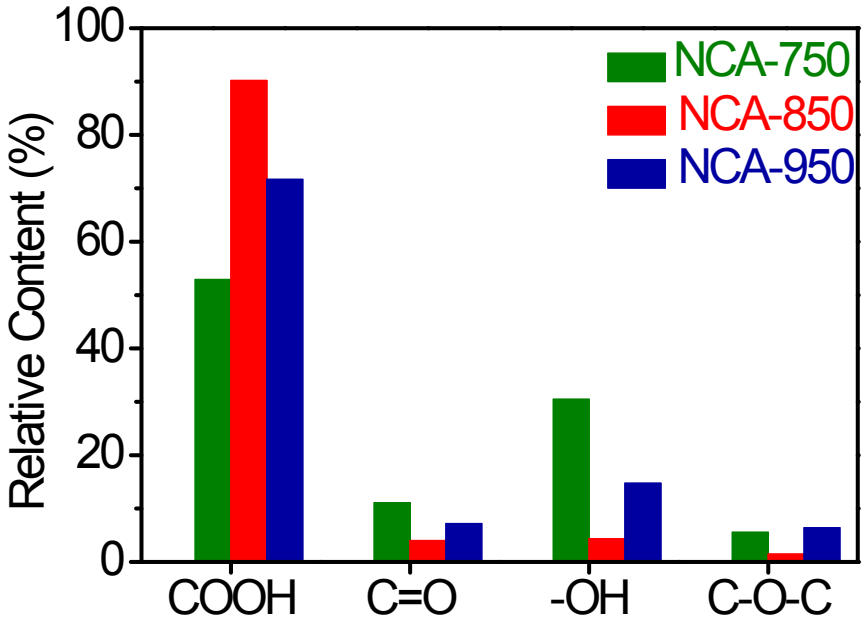

Figure S12. Relative content of deconvoluted O1s spectra for NCA-750, NCA-850 and NCA 950 samples.

The surface atomic concentration of C, N and O were calculated from the corresponding peak areas of the spectra. C 1s and N 1s spectra were acquired for further investigation of the bonding states of carbon and nitrogen atoms.

In the high resolution C 1s spectra in Figure S7 (a), S8 (a) and S9 (a), the most pronounced peak is centered at 284.5 eV, which is assigned to sp^2 C-C, followed by defects at 285.4 eV. The others peaks are assigned to the C-N (~286.2 ± 0.1 eV), O-C=O (~288.7 ± 0.1 eV) and π-π* (~290.5 ± 0.1 eV) respectively. Among these three samples, C-C accounts for about 50%, which implies a higher degree of graphitic structure. With increasing calcination temperature from 750 to 850 °C, the content of defects increased, while the concentration of C-N decreased. This means that the C-N breaks and gradually turns into defects. The presence of defects is also confirmed from the following Raman spectra.

High resolution overlapped N 1s spectra in Figure S7 (b), S8 (b) and S9 (b) are decomposed into four sub-peaks arising from pyridinic-N (~298.0 ± 0.1 eV), pyrrolic-N (~399.8 ± 0.1 eV), graphitic-N (~401.3 ± 0.1 eV) and pyridinic N^+-O^- (~402.7 ± 0.1 eV), further confirming the successful doping of N-species in these activated carbon aerogel materials. The most pronounced peak in three electrodes is pyrrolic-N and graphitic-N. With increasing the thermal etching temperature from 750 to 950°C, the content of graphitic N and pyridinic N^+-O^- decreased, while the concentration of pyrrolic N and pyridinic N increased, which is consistent with the reports of literatures.[11] Togenther with the content of nitrogen in NCA-750, 850 and 950 samples as shwon in Table S2, the conent of graphitic-N as main constituent is similar at different temperatures.

Additionally, the O 1s spectra in Figure S7 (c), S8 (c) and S9 (c) can be decomposed to three peaks due to various oxygen groups including COOH (~531.3 ± 0.1 eV), -OH (~533.0 ± 0.1 eV), C=O (~532.2 ± 0.1 eV) and C-O-C (~534.0 ± 0.1 eV) within the carbon matrix. With increasing the calcination temperature, the proportion of -COOH was firstly

increased from 52% (NCA-750) to 90% (NCA-850), and then decreased to 71% (NCA-950). In addition, the concentration of total oxygen from XPS analysis follows the same tendency (Table S2). The calculated content of –COOH was firstly increased from 5.04 wt% to 9.15 wt%, and then decreased to 5.27 wt% since the decline of surface amount of nitrogen at high temperature. This observation indicated that 850^{o}C is the optimal temperature for in-situ forming the highest concentration of –COOH.

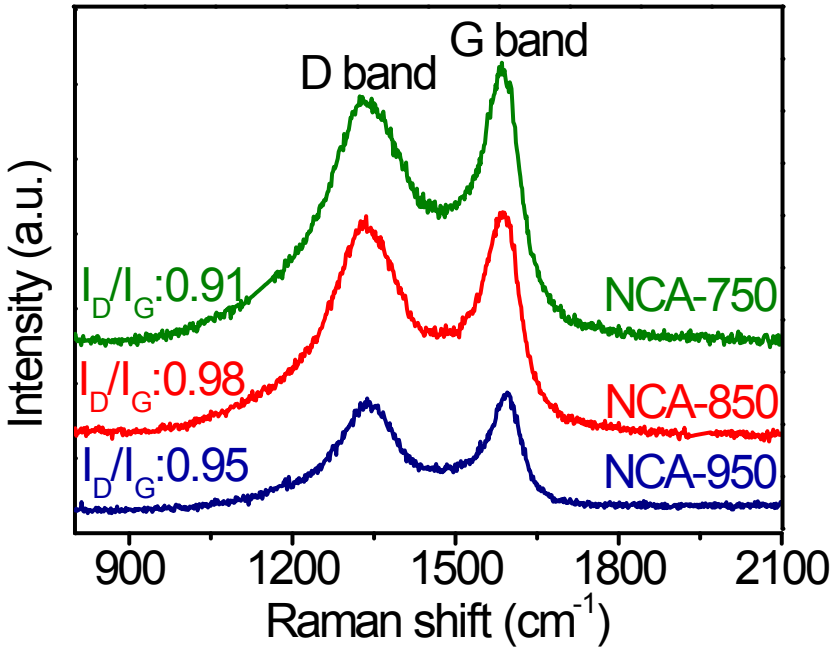

Figure S13. Raman spectra of NCA-750, NCA-850 and NCA 950 samples.

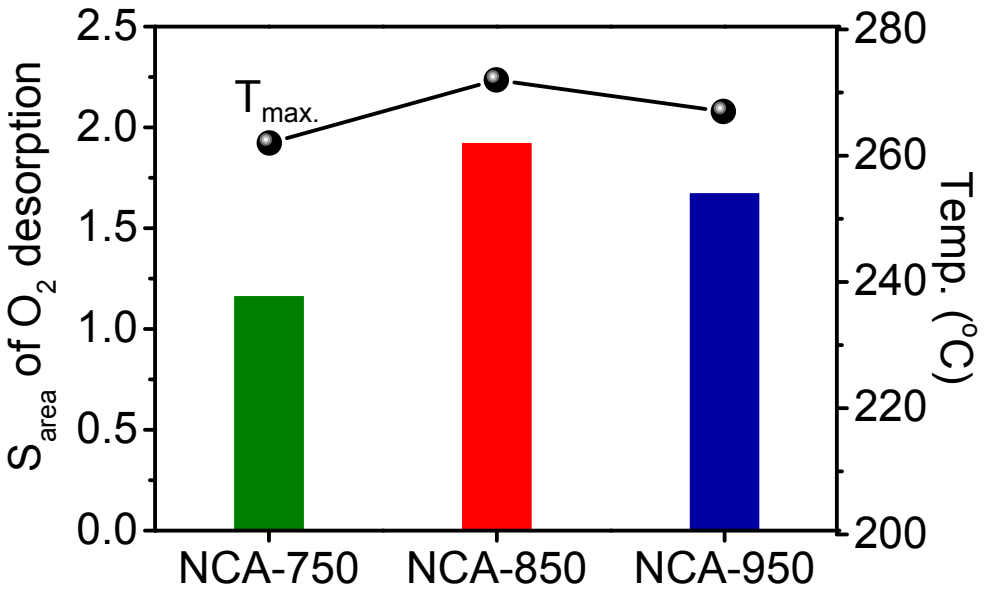

Fig S14. The peak area and maximum temperature of oxygen desorption peak for NCA-750, NCA-850 and NCA-950 in O_2-TPD spectra.

O_2-Temperature Programed Desorption (TPD) spectra of NCA electrodes confirmed the DFT sumulation that the surfical –COOH groups coupling with nitrogen enhaced the oxygen adsorption (Table S1). The area of O_2 desorption peak is positive correlation with –COOH concentration. NCA-850 exhibited the highest desorption amount of O_2 and the highest desorption temperature (maximized at 272^{o}C), indicating the strong O_2-bonded interaction with NCA-850.

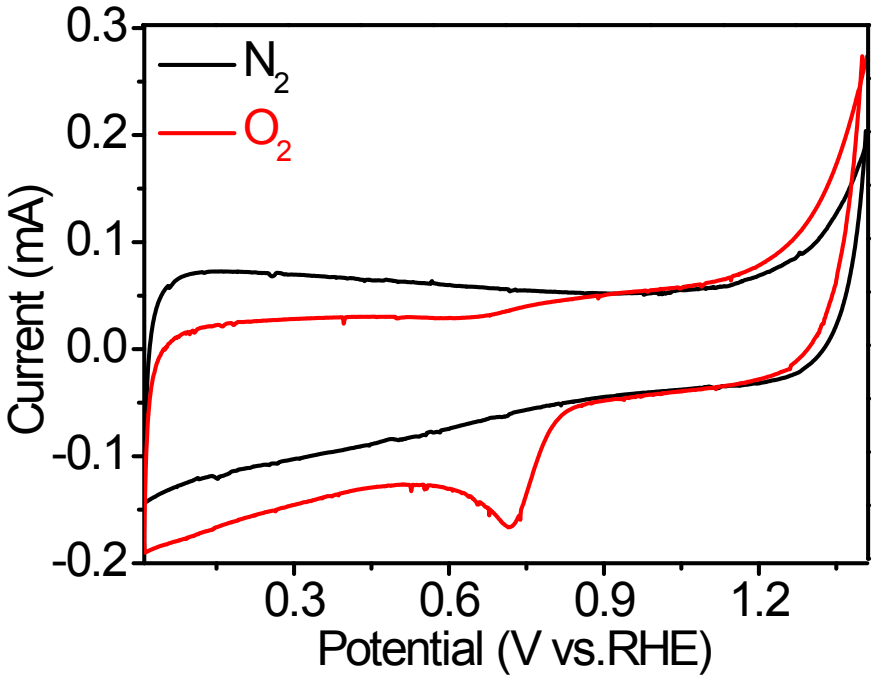

Figure S15. The cyclic voltammetry curves of NCA-850 in N_2 and O_2 atmosphere.

The CV measurement was carried out in N_2-saturated and O_2-saturated 0.1M KOH with a scan rate of 10 mV s^{-1} between 0 V to +1.4 V vs. RHE. A well-defined oxygen reduction peak at 0.72 V vs. RHE in O_2-saturated was observed, indicating the obvious ORR activity with NCA-850.

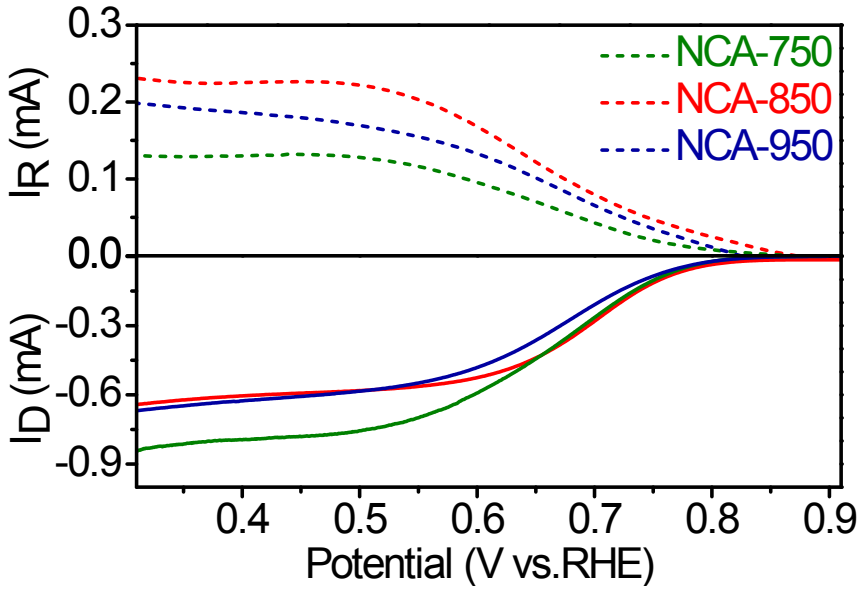

Figure S16. The ORR polarization curves of NCA-750, NCA-850 and NCA-950 at 1600 r.p.m in O_2-saturated 0.1M KOH.

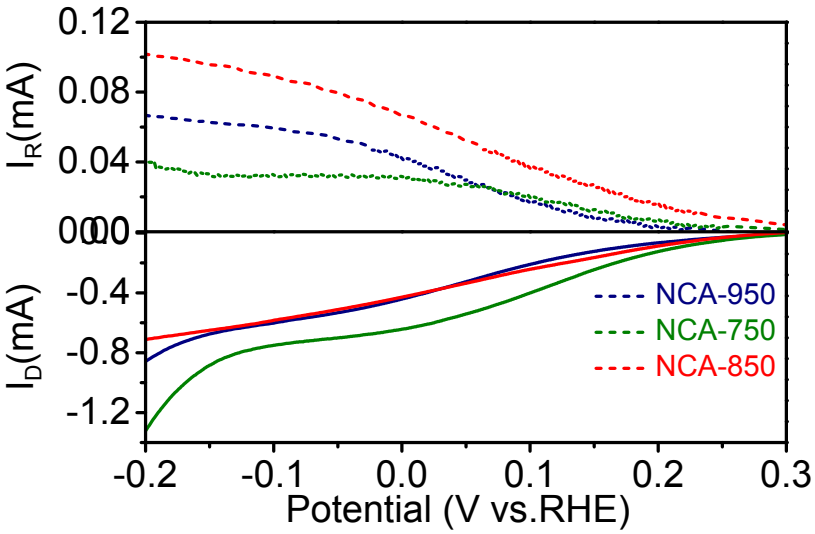

Figure S17. The ORR polarization curves of NCA-750, NCA-850 and NCA-950 at 1600 r.p.m in O_2-saturated 0.1M $HClO_4$.

Table S3. Activity and selectivity comparison of the NCA catalyst with reported carbon materials and precious metal materials for electrochemical oxygen reduction to H_2O_2.

Sample	Selectivity@0.4 V vs. RHE	Potential@ 1mA cm^{-2} vs. RHE	Loading density ($\mu g\ cm^{-2}$)	Ref
NCA-850	100%	0.7V	196	This work
O-CNTs	90%	0.7V	101	12
Fe_3O_4/carbon	60~70%	0.55V	76	13
N-doped MC	80%	0.7V	255	14
meso-BMP	<10%	--[a]	300	15
Printex L6	88%	0.5V	80	16
Pt-Hg	98%	1V	22	17
Pd-Hg/C	95%	--[a]	--[a]	18
Au-Pd	80%	0.9V	110	19
Pt-TiN	65%	1V	90	20
HPC-H24	70~95%	--[a]	318[b]	21
PD	50%	0.4V	198	22

[a] Not given in the reference

[b] The calculated H_2O_2 selectivity was evaluated from Koutecky−Levich in rotating disk electrode (RDE measurements)

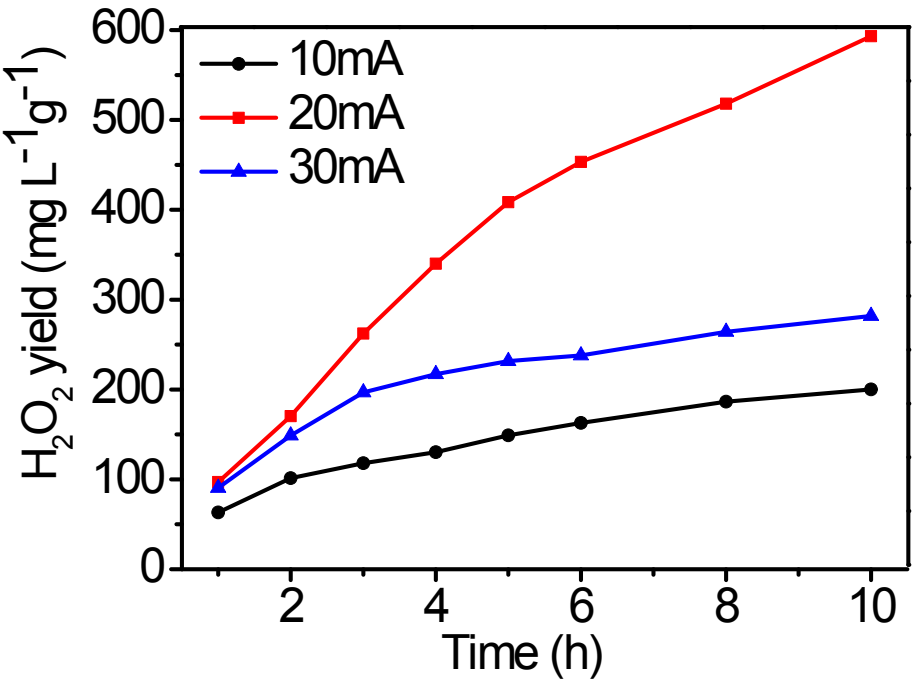

Figure S18. The real amount of electro-generated of H_2O_2 over NCA-850 at different current values.

As the current increased from 10 mA to 20 mA, the real amount of hydrogen peroxide increased from 200 $mgL^{-1}g^{-1}$ to 600 mg $L^{-1}g^{-1}$ in 10 hours. However, when it continuously increased to 30 mA, the H_2O_2 production decreased to 382 mg $L^{-1}g^{-1}$. This is because high current value favors 4-electron oxygen reduction pathway. Therefore, a current of 20mA was selected as optimal value for the electro-generation of H_2O_2 in the following experiments.

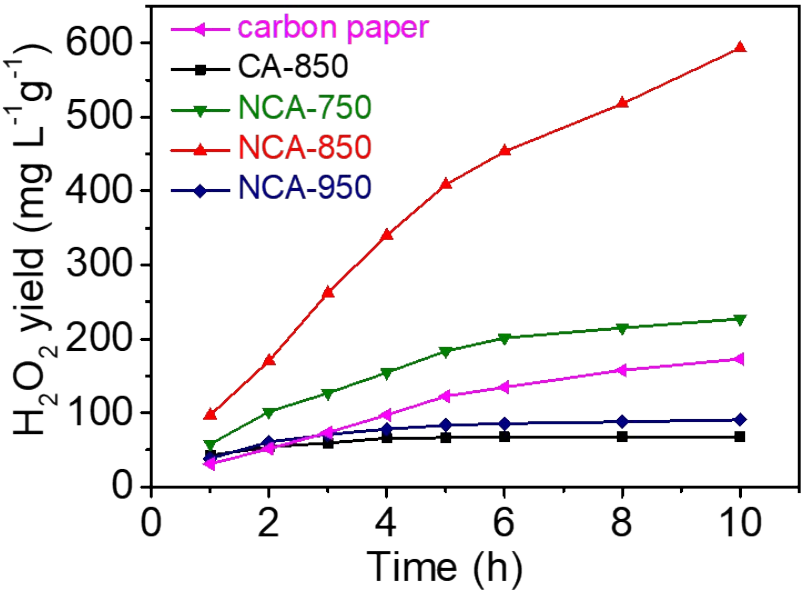

Figure S19. The real amount of electro-generated of H_2O_2 over CA-850, NCA-750, NCA-850, NCA-950 and carbon paper electrodes at the constant current value of 20 mA.

The real amount of H_2O_2 with CA-850 was only 67 $mgL^{-1}g^{-1}$. However, with the nitrogen doped, the yield of H_2O_2 was obviously improved. The H_2O_2 of NCA-850 (600 $mgL^{-1}g^{-1}$) was increased 795% compared with CA-850. Based on the above observation, NCA-850 possessed the highest concentration of –COOH groups in the presence of nitrogen dopant. In order to deeply investigate the synthetic effect of C-COOH/C-N, the real amount of H_2O_2 over NCA-x (x=750, 850 and 950 ^oC) with different content of –COOH groups was detected. With increasing the temperature, the real amount of H_2O_2 was obviously increased from 227 $mgL^{-1}g^{-1}$ (NCA-750) to 600 $mgL^{-1}g^{-1}$ (NCA-850), and then decreased to 91 $mgL^{-1}g^{-1}$ for NCA-950. Although NCA-950 has good ORR performance as shown in Figure S16, the low yield of H_2O_2 was due to surface cracking under high temperature calcination. The commercial carbon paper is recognized as a good material with the property for the production of H_2O_2. In our electrochemical hydrogen peroxide system, the actual production of H_2O_2 in carbon paper is only 173 mg $L^{-1}g^{-1}$ much lower than NCA-850.

4. References in the supporting information

1 P. E. Blöchl, *Phys. Rev. B*, 1994, **50**, 17953-17979.
2 K. B. John P. Perdew, M. Ernzerhof, *Phys. Rev. Lett.*, 1996, **77**.
3 S. Grimme, J. Antony, S. Ehrlich, H. Krieg, *J. Chem. Phys.*, 2010, **132**, 154104.
4 V. Viswanathan, H. A. Hansen, J. Rossmeisl, J. K. Norskov, *J. Phys. Chem. Lett.*, 2012, **3**, 2948-2951.
5 J. Zhang, Z. Zhao, Z. Xia, L. Dai, *Nat. Nanotechnol.*, 2015, **10**, 444-452.
6 J. R. J. K. Nørskov, A. Logadottir, and L. Lindqvist, *J. Phys. Chem. B*, 2004, **108**, 17886-17892.
7 S. Siahrostami, A. Verdaguer-Casadevall, M. Karamad, D. Deiana, P. Malacrida, B. Wickman, M. Escudero-Escribano, E. A. Paoli, R. Frydendal, T. W. Hansen, I. Chorkendorff, I. E. L. Stephens, J. Rossmeisl, *Nat. Mater.*, 2013, **12**, 1137-1143.
8 J. S. Jirkovsky, I. Panas, E. Ahlberg, M. Halasa, S. Romani, D. J. Schiffrin, *J. Am. Chem. Soc.*, 2011, **133**, 19432-19441.
9 H. Su, P. Gao, M. Y. Wang, G. Y. Zhai, J. J. Zhang, T. J. Zhao, J. Su, M. Antonietti, X. H. Li, J. S. Chen, *Angew. Chem. Int. Ed.*, 2018, **57**, 15194-15198; Z. H. Xue, J. T. Han, W. J. Feng, Q. Y. Yu, X. H. Li, M. Antonietti, J. S. Chen, *Angew. Chem. Int. Ed.*, 2018, **57**, 2697-2701.
10 H. W. Kim, M. B. Ross, N. Kornienko, L. Zhang, J. Guo, P. Yang, B. D. McCloskey, *Nat. Catal.*, 2018, **1**, 282-290.
11 T. Sharifi, G. Hu, X. E. Jia, T. Wagberg, *Acs Nano*, 2012, **6**, 8904-8912.
12 Z. Lu, G. Chen, S. Siahrostami, Z. Chen, K. Liu, J. Xie, L. Liao, T. Wu, D. Lin, Y. Liu, T. F. Jaramillo, J. K. Nørskov, Y. Cui, *Nat. Catal.*, 2018, **1**, 156-162.
13 W. R. P. Barros, Q. Wei, G. Zhang, S. Sun, M. R. V. Lanza, A. C. Tavares, *Electrochim. Acta*, 2015, **162**, 263-270.
14 V. Perazzolo, C. Durante, R. Pilot, A. Paduano, J. Zheng, G. A. Rizzi, A. Martucci, G. Granozzi, A. Gennaro, *Carbon*, 2015, **95**, 949-963.
15 F. Hasché, M. Oezaslan, P. Strasser, T.-P. Fellinger, *J. Energy Chem.*, 2016, **25**, 251-257.
16 M. H. M. T. Assumpção, R. F. B. De Souza, D. C. Rascio, J. C. M. Silva, M. L. Calegaro, I. Gaubeur, T. R. L. C. Paixão, P. Hammer, M. R. V. Lanza, M. C. Santos, *Carbon*, 2011, **49**, 2842-2851.
17 S. Siahrostami, A. Verdaguer-Casadevall, M. Karamad, D. Deiana, P. Malacrida, B. Wickman, M. Escudero-Escribano, E. A. Paoli, R. Frydendal, T. W. Hansen, I. Chorkendorff, I. E. Stephens, J. Rossmeisl, *Nat. Mater.,* 2013, **12**, 1137-1143.
18 A. Verdaguer-Casadevall, D. Deiana, M. Karamad, S. Siahrostami, P. Malacrida, T. W. Hansen, J. Rossmeisl, I. Chorkendorff, I. E. Stephens, *Nano Lett.*, 2014, **14**, 1603-1608.
19 J. S. Jirkovsky, I. Panas, E. Ahlberg, M. Halasa, S. Romani, D. J. Schiffrin, *J. Am. Chem. Soc.*, 2011, **133**, 19432-19441.
20 S. Yang, J. Kim, Y. J. Tak, A. Soon, H. Lee, *Angew. Chem. Int. Ed.*, 2016, **55**, 2058-2062.
21 Y. Liu, X. Quan, X. Fan, H. Wang, S. Chen, *Angew. Chem. Int. Ed.*, 2015, **54**, 6837-6841.
22 O. L. Li, S. Chiba, Y. Wada, G. Panomsuwan, T. Ishizaki, *J. Mater. Chem. A*, 2017, **5**, 2073-2082